1 **Cryo-Electron Tomography 3D Structure and Nanoscale Model of *Arabidopsis***

2 ***thaliana* Cell Wall**

3 Authors: **Purbasha Sarkar[1, 2, †], Michal Kowalczyk[1,2,3], Salil Apte[1], Edgar G.**

4 **Yap[1], Jyotirmoy Das[1], Paul D. Adams[1, 2], Chandrajit Bajaj[4], Pablo Guindos[5, 6,]**

5 **[7], Manfred Auer[1, 2*]**

6 **Affiliations:**

7 [1]Molecular Biophysics and Integrated Bioimaging Division, Lawrence Berkeley National

8 Laboratory, Berkeley, CA 94720, USA

9 [2]Joint BioEnergy Institute, Lawrence Berkeley National Laboratory, Berkeley, CA 94720, USA

10 [3]School of Engineering & the Built Environment, Napier University, Edinburgh, UK

11 [4]Department of Computer Science, University of Texas, Austin Texas 78712

12 [5]Department of Structural and Geotechnical Engineering, Pontificia Universidad Católica de

13 Chile, 4860 Santiago, Chile

14 [6]Department of Engineering and Management of Construction, Pontificia Universidad Católica

15 de Chile, 4860 Santiago, Chile

16 [7]UC Timber Innovation Center, Pontificia Universidad Católica de Chile, 4860 Santiago, Chile

17

18 * Correspondence to: mauer@lbl.gov

19 † Current address: Reliance Industries Ltd., Navi Mumbai - 400701, India

20

21

22

23   **Abstract**:

24   Using cryo-electron tomography of vitrified sections of one month-old *Arabidopsis thaliana*

25   inflorescence stem tissue, we visualized primary and secondary cell walls of xylem tissue.

26   Extensive quantitative and statistical analysis of segmented 3D tomographic data allowed

27   geometrically idealized 3D-CAD model building of prototypic microfibrils, cross-links, and their

28   supramolecular microfibril 3D organization. We propose a prototypic microfibril model where a

29   cellulose core is heavily decorated by a thin sheath of hemicellulose with infrequent but sturdy

30   hemicellulose-based cross-links. Such prototypic microfibrils then adopt a rather unexpected 3D

31   supramolecular organization of high order and complexity. We discuss a possible new role for

32   lignin in plant cell walls at low concentrations with lignin not acting as a matrix but rather as a

33   reinforcement of microfibrils and cross-links. Extensive computational simulations of

34   mechanical properties further revealed that this 3D organization of the cell wall is not optimized

35   for load bearing but instead for flexibility and ductility.

36

37   **One Sentence Summary:**

38   Cryo-electron tomography and mechanical simulations revealed cell wall 3D architecture,

39   optimized for flexibility/ductility.

40

41   Cell walls provide mechanical strength and protection to plants, while being flexible to

42   support their growth and development and have been studied for over eight decades (1-6). The

43   current model of plant cell walls portrays a framework of ~3.5 nm thick cellulose microfibrils,

44   interconnected by single-strand hemicellulose thus forming a rather loose 3D "long-tether"

45   network, with hemicellulose adhering to significant stretches of the microfibrils (7-14). Other

46   prominent cell wall components, pectins are predominantly found in the middle lamella (ML)

47   adhering two adjacent cells (15), whereas phenolic lignin polymers are thought to form a

48   hydrophobic matrix in between the cellulose-hemicellulose network (15, 16). The most

49   commonly discussed cell wall model has microfibrils alternating between two sharply distinct

50   orientations, not unlike textile fabric (3, 7, 11), however alternative models have been proposed

51   (1-2, 17-19).

52   Numerical simulation of mechanical properties using approximation techniques such as

53   the finite element method (20) require realistic 3D cell wall structures and models, and to date

54   have been based on the assumption of pseudo-random fiber networks (21-23). Model building

55   allows virtual testing of the different cell wall components and alternative 3D configurations. As

56   for fiber-reinforced composites, homogenization techniques can be combined with finite element

57   methods to extract global properties such as stiffness of the wall.

58   Here we used cryo-electron tomography vitreous sections of 1-month old *Arabidopsis*

59   *thaliana* inflorescence stems (24) to reveal the 3D nano-architecture of microfibrils and their

60   cross-connectors, as well as the supramolecular 3D organization of primary and secondary walls.

61   Extensive statistical volumetric analysis and model building, followed by mechanical properties

62   simulations suggest that the secondary cell walls we examined are not optimized for maximal

63 load bearing but instead for flexibility and ductility with superior load transfer capabilities as

64 well as elastic and viscoelastic energetic capacities.

65

66 **Cell Wall Building Blocks**

67   1-month old *Arabidopsis thaliana* inflorescence stems (Fig. 1A-B) have different cell

68 wall types (Fig. 1C), including thin xylem parenchyma (XP) cell walls with only primary walls

69 and thick xylem tracheary (XTE) elements cell walls with both primary and secondary walls.

70 Figure 1D and 1E show single ~1nm thin slices through 3D reconstruction of vitreous sections of

71 XP and XTE cell walls cut from self-pressurized, ultra-rapidly frozen young stem segments (24),

72 with corresponding 3D renderings shown in Fig. 1F and 1G, respectively.

73   Measuring the diameter of individual microfibrils (Fig. 2A, n=150 for each cell wall

74 type), we observed peaks at 3.5 ± 0.5 nm and at 5 ± 0.5 nm (Fig. 2B), which in accordance with

75 the current microfibril model, may correspond to a round cellulose core that in many places is

76 surrounded by a very thin sheath of hemicellulose. Some microfibrils appear elliptical with up to

77 ~9 nm thicker portions (Fig. 2B-C) that may be assigned to additional hemicellulose, pectin, or

78 lignin. This assignment was further supported by the experimental removal of pectins and

79 hemicelluloses (24-25) from primary cell walls (Ext. PCW) by treatments with 0.5% ammonium

80 oxalate and 4% NaOH prior to dehydration and resin-embedding (Fig. 2B). Cellulose,

81 hemicellulose and pectin cannot be directly distinguished in the density maps due to their

82 chemical similarity. We will use the term matrix polychaccarides instead of hemicellulose, since

83 pectin's contribution to microfibrils and cross-links cannot be ruled out, despite the overall low

84 pectin concentration and expected localization of pectin to the middle lamella.

85   Statistical analysis of microfibrils and cross-connector thickness allowed a comparison

86   between the volumes occupied by cellulose and matrix polysaccharides, respectively, and to

87   build idealized models: one where microfibrils are exclusively made of cellulose, with all matrix

88   polysaccharides residing in the cross-links only (Fig. 2D) and another scenario where cellulose

89   strands form a 3.5 nm microfibril core, surrounded by a thin matrix polysaccharides-based sheath

90   and matrix polysaccharides form sturdy cross-links (Fig. 2E). The matrix polysaccharides-to-

91   cellulose volume ratio of the first scenario is ~0.07 and 1.3 for the second scenario, which is in

92   good agreement with bulk analysis estimates from *Arabidospsis thaliana* root and leaves (26).

93   While we realize the limitations of comparison with bulk mass ratio biochemical analysis, our

94   core-and-sheath model seems more likely, and is agreement with previous findings that

95   significant stretches of matrix polysaccharide strands are closely aligned with the elementary

96   fibril cellulose core (9, 10, 12, 27-28). This arrangement would allow hemicellulose sheaths and

97   cross-links to slide along the cellulose core under shear force, whereas rigid, highly localized

98   connections would likely break and has significant implications for force transmission between

99   adjacent microfibril layers as will be discussed below. Bridge-like cross-linkers (n=100 for each

100   type of cell wall) appeared short (typically 4-6 nm) and thick, indicating bundling of multiple

101   matrix polysaccharide strands. Within the z=50 nm section-height examined in cryo-tomograms,

102   we found on average for 4 and 3 out of every 5 microfibrils for PCWs and SCWs, respectively.

103   Cross-links were absent in chemically extracted PCWs (Fig. 2F).

104

105   **Supramolecular 3D Cell Wall Organization**

106   As shown in Figure 3A-B xylem tracheary element (XTE) cells feature multiple layers, with the

107   middle lamella (M) being sandwiched between primary cell wall layers (P), which are flanked by

5

108   three secondary cell wall segments (S1, S2, S3) on one side and one (S) secondary cell wall

109   segment on the other side, with intermittent transition zones (T). Xylem parenchyma (XP) cells

110   lack secondary cell walls layers (Fig 3C-D). To determine whether texture differences across the

111   cell wall visible in cryo-EM projection images of XTE cell walls (Fig 3A) could be attributed to

112   differences in microfibril 3D orientations, we measured the average tilt angle of microfibrils in

113   consecutive radial microfibril layers . We found in each of the S1, S2 and S3 regions of SCWs

114   ~15 consecutive parallel microfibril layers (Fig. 3B) that were off-set from axial orientation by

115   either plus or minus ~27˚ (with slight variations being present in the tilt angle value for each

116   microfibril). Between each of the S regions and between the S and P region, we found a three-

117   layer transition zone (T), where microfibrils were oriented axially. Likewise, in primary cell

118   walls in both XTE and XP cells (Fig. 3C-D) most microfibrils were oriented axially (parallel to

119   the growth axis).

120

121   **Mechanical Cell Wall Properties**

122   To determine what effect the supramolecular 3D organization had on the mechanical

123   properties of primary and secondary cell walls, we resorted to computational simulations (Fig.

124   4). First we examined the mechanical properties of the rather complex tomography-derived 3D

125   volume of the complex XTE walls (Fig. 4A) and of simplified and idealized 3D-CAD models

126   (Fig. 4B), which allowed for the calculation of axial load and shear forces for different wall

127   models. We estimated the overall mechanical stiffness on both the experimentally determined

128   volumes (Fig. 4C) and CAD-model idealized models (Fig. 4D), using homogenization, as is a

129   routine approach in composite and porous material research.

130   ***Mechanical properties of tomographic cell wall density maps***

6

131   We assumed a 300x100x50nm^3 tomographic representative volume element (RVE) of SCW to

132   be made of orthotropic material (Supplementary text; Tables S1 and S2), and considered

133   Young's modulus of 30 and 10 GPa for cellulose and hemicellulose, respectively (21). We found

134   the effective stiffness of the SCW tomographic volume (SCW-Tomo) to be E_R=5.6 MPa, E_T=25

135   MPa and E_L=59 MPa, along the principal material axes (radial, transverse, longitudinal)

136   respectively (Fig. 4E). Likewise, we also performed a mechanical analysis of the PCW

137   tomographic volume (PCW-Tomo), and found the stiffness to be E_R=63 MPa, E_T=161MPa and

138   E_L=521MPa (Fig 4E). We attribute the higher stiffness of the PCW-Tomo compared to the

139   SCW-Tomo to a smaller void fraction, which was surprisingly large (PCW: ~72%; SCW:

140   80%). The void volume is the space not taken up by microfibrils or cross-links, which is likely

141   filled with water and soluble small molecules. Our cryo-tomographic analysis suggested the

142   absence of an extensive lignin network matrix, as oligomers or polymers larger than 3 nm should

143   be visible in our cryo-tomograms. We modeled lignin as ball-like objects ranging from 0.5-3 nm

144   to be added into the SCW-Tomo volume at various concentrations from 0-30% of the total

145   volume fraction (Fig. S2 A) and found that at low lignin concentrations there wasn't enough

146   material to form a continuous matrix, instead lignin may reinforce the cellulose-hemicellulose

147   macromolecular network, as even small increases in lignin concentrations has significant effects

148   on the Young moduli, which showed quadratic increases in all directions (Fig. S2G). We submit

149   that the role of lignin at low concentrations is not to act as a matrix but to reinforce the

150   microfibril-marix polymer framework, thus enhancing cell wall's overall stiffness.

151

152   ***Comparison idealized 3D-CAD model with tomographic density maps***

153   We considered four idealized modeling approaches (see Supplemental material and Fig.

154   S1) to both primary and secondary cell wall, and chose the NET model for further simulations.

7

155   The calculated stiffness in SCW-NET (E_R=4MPa, E_T=9 MPa, E_L=1520 MPa) was in good

156   agreement with the homogenized SCW-Tomo results, except for the stiffness in the axial

157   direction, which was ~25 fold higher (Fig. 4E). This discrepancy led us to an in-depth

158   examination of microfibril shapes. We realized that microfibrils were not straight rods but had a

159   wavy appearance, which corresponds to a weakening of the microfibril in the axial direction. To

160   model such imperfections we introduced a tortuosity (twist) in our idealized microfibril model,

161   which had a very small influence in the transverse direction (E_R=4.5 MPa, E_T=9.2 MPa), but

162   resulted in stiffness drop in the axial direction (E_L=63 MPa), bringing it in close agreement with

163   the SCW-Tomo results in all three directions (Fig. 4E).

164   Nonlinear buckling and viscoelastic analyses of the fibers with and without tortuosity

165   (Fig. 4F) revealed that that tortuous fibers withstand ~50 times lower buckling load compared to

166   straight fibers (Fig. 4G-H) but can undergo ~9-times larger deformations before collapse and

167   store up to 43% more elastic energy as they deform. We hence, conclude that imperfections in

168   microfibril structure, while significantly reducing the stiffness of the cell wall, increases its

169   ductility as well as the dissipation of elastic and viscoelastic energies, which could be crucial for

170   plants to prevent breakage against extreme loading (such as in high winds).

171   ***Supramolecular 3D organization of microfibrils across the cell wall***

172   We further examined the effect of the alternation of microfibril orientation (plus 27˚ or

173   minus 27˚) for each of the three 15-microfibril layers in the S1, S2 and S3 SCW and the 3-layer

174   transition zone in axial microfibril orientation (Fig. S3A). The minus/plus/minus 27˚ deviation

175   from an axial orientation caused a dramatic stiffness drop in the axial direction, but also a 200-

176   fold increase in the elastic strain energy density. Without transition zones (18 layers that are

177   minus/plus/minus 27˚ inclined, Fig. S3B), axial stiffness was further reduced by a factor of 4,

178   with an increased elastic energy storage of 30%, whereas if all microfibrils (54 layers) were

179   inclined by 27˚ (Fig. S3C), axial stiffness decreased 27-fold and elastic energy storage increased

180   by 800%. The observed minus/plus/minus configuration is a quasi-symmetric and balanced

181   composite (each ply has an opposite-aligned counterpart), thus decoupling membrane (in-plane)

182   and bending (out-of-plane) cell wall mechanical responses (29). This could be vital for plants to

183   prevent cell deformation during growth and external loading.   Spiral spring-like configurations,

184   e.g. in cylindrical spiral reinforced concrete columns (30), are found in civil, mechanic,

185   automotive and aerospace engineering for their superior ductility and outstanding energy

186   absorption capacity of impact loads, mainly due to multiple failure mechanisms (31).

187

188

189

190

191   **LITERATURE CITED**

192   1. Van Iterson, G., 1937. A few observations on the hairs of the stamens of *Tradescantia*
193   *virginica*. Protoplasma 27: 190–211.
194   2. Roelofsen, P.A. and Houwink, A. L. 1951. Cell wall structure of staminal hairs of
195   *Tradescantia virginica* and its relation with growth. Protoplasma 40: 1–22.
196   3. Roelofsen, P. A., 1958. Cell-wall structure as related to surface growth. Some
197   supplementary remarks multinet growth. Acta. Bot. Neerl. 7: 77–89.
198   4. Ohad I, Danon D (1964) On the dimensions of cellulose microfibrils. J Cell Biol 22: 302-
199   305
200   5. Frey-Wyssling A (1968) The ultrastructure of wood. Wood Sci Technol 2: 73-83

201   6. Heyn AN (1969) The elementary fibril and supermolecular structure of cellulose in soft

202   wood fiber. J Ultrast Res 26: 52-68

203   7. Somerville, C., Bauer, S., Brininstool, G., Facette, M., Hamann, T., Milne, J., Osborne, E.,

204   Paredez, A., Persson, S., Raab, T., Vorwerk, S. and Youngs, H. 2004. Toward a systems

205   approach to understanding plant cell walls. Science 306: 2206-2211.

206   8. Cosgrove, D. J. 2005. Growth of the plant cell wall. Nature rev. Molecular cell biology 6:

207   850-861.,

208   9. Ding, S-Y. and Himmel, M. E. 2006. The maize primary cell wall microfibril: a new model

209   derived from direct visualization. J. Agri. Food Chem. 54: 597-606.;

210   10. Ding SY, Liu YS, Zeng Y, Himmel ME, Baker JO, et al. (2012) How does plant cell wall

211   nanoscale architecture correlate with enzymatic digestibility? Science 338: 1055-1060

212   11. McCann, M. C. and Roberts, K. 1991. Architecture of the primary cell wall. Academica

213   Press, London, UK

214   12. Rose, J. K. C. and Bennett, A. B. 1999. Cooperative disassembly of the cellulose xyloglucan

215   network of plant cell walls: parallels between cell expansion and fruit ripening. Trends Plant

216   Sci. 4: 176-183.

217   13. Newman, R. H., Hill, S. J. and Harris, P. J. 2013. Wide-angle x-ray scattering and solid state

218   nuclear magnetic resonance data combined to test models for cellulose microfibrils in mung

219   bean cell walls. Plant Phys 163: 1558-1567

220   14. Thomas, L. H., Forsyth, V. T., Sturcová, A., Kennedy, C. J., May RP, Altaner, C. M.,

221   Apperley, D. C., Wess, T. J. and Jarvis, M. C. 2013. Structure of cellulose microfibrils in

222   primary cell walls from collenchyma. Plant Physiol. 161: 465–476.

223   15. Sarkar, P., Bosneaga, E. and Auer, M. 2009. Plant cell walls throughout evolution: towards

224   a molecular understanding of their design principles. Journal of Experimental Botany 60:

225   3615-3635.

226   16. Banasiak, A. 2014 Evolution of the cell wall components during terrestrialization Acta Soc

227   Bot Pol 83(4):349–362

228   17. Llyod C. 2011. Dynamic microtubules and the texture of plant cell walls. Int. Rev. Cell Mol.

229   Biol. 287: 287-329.

230   18. Sarkar, P. and Auer, M. (2016) Organization of the plant cell wall, In: Molecular cell

231   biology of the growth and differentiation of plant cells, Rose, R. J [Ed.]: 101-119

232   19. Park, Y. B. and Cosgrove, D. J. 2012. A revised architecture of primary cell walls based on

233   biomechanical changes induced by substrate-specific endoglucanases. Plant Physiol. 158:

234   1933-1943

235   20. Zienkiewicz, Olgierd Cecil, et al. The finite element method. Vol. 3. London: McGraw-hill,

236   1977.

237   21. Kha H, Tuble SC, Kalyanasundaram S, Williamson RE (2010) WallGen, software to

238   construct layered cellulose-hemicellulose networks and predict their small deformation

239   mechanics. Plant Physiol 152: 774–786

240   22. Yi, H., & Puri, V. M. (2012). Architecture-based multiscale computational modeling of

241   plant cell wall mechanics to examine the hydrogen-bonding hypothesis of the cell wall

242   network structure model. Plant physiology, 160(3), 1281-1292.

243   23. Nili, A., Yi, H., Crespi, V. H., & Puri, V. M. (2015). Examination of biological hotspot

244   hypothesis of primary cell wall using a computational cell wall network

245   model. Cellulose, 22(2), 1027-1038.

246   24. Sarkar, P., Bosneaga, E., Yap, E. G. Jr., Das, J., Tsai, W-T., Cabal, A., Neuhaus, E., Maji,

247   D., Kumar, S., Joo, M., Yakovlev, S., Csencsits, R., Yu, Z., Bajaj, C., Downing, K. H. and

248   Auer, M. 2014. Electron Tomography of Cryo-Immobilized Plant Tissue: a novel approach

249   to studying 3d macromolecular architecture of mature plant cell walls in situ. PLoS ONE, 9:

250   e106928.

251   25. The ultrastructural demonstration o/ compounds containing 1,2-glycol groups in plant cell

252   walls G. G. JEWELL and c . A. SAXTON Histochemical Journal, 2 (I97O), 17-27

253   26. Zablackis E, Jing H, Muller B, Darvill AG, Albersheim P: Characterization of the cell-wall

254   polysaccharides of Arabidopsis thaliana leaves. Plant Physiol 1995, 107:1129-1138.

255   27. Busse-Wicher M, Gomes TC, Tryfona T, Nikolovski N, Stott K, Grantham NJ, Bolam DN,

256   Skaf MS, Dupree P. The pattern of xylan acetylation suggests xylan may interact with

257   cellulose microfibrils as a twofold helical screw in the secondary plant cell wall of

258   Arabidopsis thaliana. Plant J. 2014; 79:492–506

259   28. Simmons TJ, Mortimer JC, Bernadinelli OD, Poeppler AC, Brown SP, deAzevedo ER,

260   Dupree R, Dupree P. Folding of xylan onto cellulose fibrils in plant cell walls revealed by

261   solid-state NMR. Nature Communications 2016; 13902

262 29. Bailie, J. A., Ley, R. P., & Pasricha, A. (1997). A summary and review of composite laminate design guidelines, Northrop Grumman Report under NASA Contract NAS1-
264   19347.

265 30. Park, Robert, and Thomas Paulay. Reinforced concrete structures. John Wiley & Sons, 1975.

267 31. Yan, Libo, and Nawawi Chouw. "Crashworthiness characteristics of flax fibre reinforced epoxy tubes for energy absorption application." Materials & Design51 (2013): 629-640.

269

270

271 **Acknowledgement:**

284
285 The authors declare no financial and non-financial competing interests.

286 **FIGURE LEGEND:**

287 **Fig 1.** Cryo-electron tomography of thick xylem tracheary elements cell walls and thin xylem

288 parenchyma. A) 1 month-old *Arabidopsis thaliana* inflorescence stem tissue. The white box

289 marks a stem segment that was taken for cryo-electron tomography. B) Cross-section through

290 the stem showing the different tissue and cell types in the stem. The black box marks a tissue

291 region similar to the one used for cryo-EM imaging. Note that the section displayed is a Toluene

292 Blue-stained semithin section cut from a high-pressure frozen, freeze-substituted and resin-

293 embedded samples imaged by optical light microscopy in order to provide an overview of the

294 tissues and cells in the plant stem organ. Scale bar = 50 µm. C) Electron micrograph of a ~25 µm

295 by ~25 µm tissue region of interest showing both a thick xylem tracheary elements cell wall (left

296 box) and a thin xylem parenchyma cell wall (right box). Scale bar = 5 µm. D) Zero degree

297 projection view cryo-electron microscopy of thick xylem tracheary elements cell wall, containing

298 primary and secondary cell wall. E) Zero-degree projection view cryo-electron microscopy of

299 thin xylem parenchyma cell wall, containing only primary cell wall. F) 3D rendering of a ~50 nm

300 thin slab of a cryo-tomogram of xylem tracheary elements cell wall. G) 3D rendering of a ~50

301 nm thin slab of a cryo-tomogram of xylem parenchyma cell wall. Scale bars = 100 nm.

302

303 **Fig 2.** Statistical analysis based 3D modeling of microfibrils and cross-links A) 3D rendering of

304 two neighboring microfibrils in the cryo-tomogram. Scale bar = 5 nm. B) Plot of the statistical

305 analysis of the frequency of microfibril diameter reveals a peak at 3.5 nm and 5-5.5 nm, and a

306 small shoulder to dimensions up to 9 nm. C) Gallery of 3 different microfibrils cross-sections

307 illustrating the numbers obtained in Fig 4B) with microfibrils being round at ~3.5 nm (middle

308 panel), oval shaped with a diameter of ~3.5 nm by ~5-5.5 nm (left panel), reaching up to 9-10

13

309   nm (right panel). Scale bars = 2 nm. D) Hypothetical 3D-CAD model with all of cellulose

310   residing in the microfibrils and hemicellulose confined to cross-links only. E) Alternative 3D

311   model of two adjacent microfibrils (middle) that contain a cellulose core (left), surrounded by a

312   hemicellulose sheath as well as a cross-connection between adjacent microfibrils (right). F)

313   Occurrence of cross-links in PCW (left), SCW (middle) and chemically extracted PCW (right).

314   Scale bars = 5 nm.

315

316   **Fig 3.** Supramolecular 3D organization of microfibrils in xylem tracheary elements and xylem

317   parenchyma cell walls. A) Zero-degree projection image of xylem tracheary elements cell wall,

318   showing two adjacent cells with both secondary and primary cell walls. Note that one of the two

319   adjacent cells has several secondary cell wall subregions, called S1, S2 and S3 and transition

320   zones (T). On the other side of the middle lamella (M) is the primary cell wall P, a transition

321   zone T as well as one secondary cell wall region.Scale bar = 100 nm. B) Idealized model of a

322   xylem tracheary elements cell wall at side view (top), slanted 45° view (middle) and an en-face

323   view of microfibrils (bottom). Note that microfibril orientation differs in S1, S2 and S3, with 15

324   layers of microfibril featuring an average angle of minus ~27°, plus ~27° and minus ~27° off the

325   longitudinal axis (plant elongation direction). S3, S2, S1 and the Primary Cell Wall (PCW)

326   regions are separated by a three layer-transition zone with axial microfibril orientation. The

327   pectin-rich middle lamella is depicted in the idealized model as a single plane separating the cell

328   walls of two adjacent cells. C) Zero-degree projection image of xylem parenchyma cell walls,

329   showing two adjacent cells with only primary cell walls. Scale bar = 100 nm. D) Idealized

330   model of a xylem parenchyma cell wall at side view (top), D2) slanted 45° view (middle) and an

331   en-face view (bottom). Note that in PCW microfibril orientation is mostly axial.

14

332

333   **Fig 4.** Computational analysis of cell wall mechanical properties. (A, B) Supramolecular

334   structure segmented from the tomographic reconstruction (A) and a geometrically idealized cell

335   wall model (B) both including only the S1-T-S2-T-S3 portions of the idealized model. (C, D)

336   Deformation of the cell wall under radial pressure, for both the segmented volume (C) as well as

337   an idealized model (D), revealing a linear distribution of force throughout the secondary cell

338   wall. (E) Graphic depiction of the Young elastic moduli (radial, longitudinal and tangential) for

339   primary cell walls, secondary cell wall regions segmented from the tomographic 3D data as well

340   as idealized models of the secondary cell walls, before and after introduction of tortuosity. (F, G,

341   H) Load bearing behavior of microfibrils under buckling due to axial stress, revealing significant

342   decrease of failure load but very high increase of ductility (F), when moving from an idealized

343   straight microfibril (G) to a tortuous fiber (H).

344

345

346   **Supplementary Materials:**

347   **Fig S1.** Choice of Modeling Approach. We considered four idealized modeling approaches: (A)

348   NET is a network model that fully accounts for the 3D volume of both microfibrils and cross-

349   links B) BEAM is a simplified approach based on Timoshenko beam mechanical theory (C)

350   NETMAT is similar to NET, with an added a matrix in between the fibers and (D) MAT, which

351   is similar to NETMAT but does not contain inter-microfibrillar cross-connectors.

352   **Fig S2.** Modeling of lignin distribution in secondary cell wall (A, D) Secondary cell wall with an

353   assumed 0% lignin. 20% of the total volume available is occupied by the cellulose/hemicellulose

354   network. (A) overview (D) close-up detail. (B, E) 5% total volume of lignin (equivalent to a 15-

355   20% dry weight) is added to the segmented map displayed in A. (B) overview and (E) close-up

356   detail reveal vast amount of space remains unoccupied, inconsistent with a dense matrix in which

357   microfibrils are embedded and thus mechanically connected. Increasing the lignin to 10% of total

358   volume (resulting in a ~30-35% dry weight) leads to much more densely connected network,

359   which is consistent with a matrix at these much higher lignin content. (C) overview (F) close-up

360   detail. Note that the corresponding dry-weight is an estimate making assumptions on similarity in

361   density of lignin and cellulose/hemicellulose matrix. (G) Comparison of elastic moduli for radial

362   (E_r), tangential (E_t) and longitudinal (E_L) force loading.

363   **Fig S3.** Hypothetical XTE cell wall models with varying supramolecular organization. A) Cell

364   wall model with 15 microfibril layers each in the S1, S2 and S3 SCW that were inclined minus

365   27˚, plus 27˚ and minus 27˚, respectively, and that were separated from each other by a 3

366   microfibril layer transition zone with axial microfibril orientation. B) Cell wall model without

16

367   transition zones, and 18 layers of microfibrils that are minus/plus/minus 27˚ inclined. C) All

368   microfibrils (54 layers) are all inclined by 27˚.

369

370   **Table S1.** Differences on the calculated properties calculated by homogenization method on
371   differently sized density map fragments.
372

Size of the Density Map Fragment Used on the Calculation ([nm^3]		Absolute Difference Between RVE A and RVE B on the Calculated Mechanical Properties (%)
RVE A	RVE B	
200x200x50	300x100x50	40
300x100x50	400x350x50	15
300x100x50	300x300x100*	13
300x100x50	300x300x200*	12

373
374
375
376   **Table S2.** Average strain equivalence errors of the different elastic laws used in homogenization.
377

Elastic Constitutive Law Used in Homogenization	Average Strain Equivalence Error
Isotropy	67%
Transverse isotropy	20%
Orthotropy	6%

378
379

380 **SUPPLEMENTAL MATERIAL**

381

382 **Materials and Methods:**

383 **Plant Material:** Wild type *Arabidopsis thaliana* (Arabidopsis) seeds from the Colombia ecotype

384 (Col 0) were sterilized in 30% bleach, 0.02% Triton and vernalized at 4 ºC in water for 48 hours.

385 They were germinated on 0.7% agar plates containing 0.5x Murashige and Skoog medium for 10

386 d at 21 ºC under continuous light in a growth chamber. The seedlings were then transferred to

387 pots containing soil mixture and placed in a growth chamber programmed for a 16 h light/8 h

388 dark cycle at 21 ºC. Stem tissue from ~1 month old plants that had newly growing inflorescence

389 stems (2-3 cm long) were used for electron tomography. Stem segments from freshly collected

390 samples were used for electron tomography.

391

392 **Cryo-electron tomography of *Arabidopsis thaliana*:** ~2 mm long stem segments of *Arabidopsis*

393 *thaliana* (Col 0) were frozen in sealed copper capillary tubes in 20% dextrane by self-pressurized

394 rapid freezing method (32) and sectioned at -160ºC using a Leica EMUC7 ultramicrotome with a

395 Leica EM FC7 cryo chamber attachment (Leica Microsystems Inc.). Ribbons of nominal ~90 nm

396 ultrathin cryo-sections were manipulated by hand with an eye lash and placed onto carbon-coated

397 lacey formvar grids and attached to the grids using a Leica EM CRION ionizer. Single-axis cryo

398 tilt series were collected from -60° to +60° with 2° increments under low dose conditions on two

399 different set-up. Some datasets were collected on a Tecnai F20 TEM (Thermofisher, Inc,

400 Hillsboro, OR, USA) with a 4K x 4K Gatan Ultrscan 4000 CCD camera (Gatan Inc., Pleasanton,

401 CA, USA) and Leginon (33) at 120 kV and a voxel size of 0.44 nm. Other datasets were collected

19

402 on a JEOL JEM–3100FFC TEM (JEOL Ltd, Akishima, Tokyo, Japan) equipped with a field

403 emission gun electron source operating at 300kV, an in-column Omega energy filter (JEOL), a

404 cryo- transfer stage and a Gatan 795 2Kx2K CCD camera and SerialEM (34) and a voxel size of

405 1.1 nm voxel size. Images were aligned by patch-tracking method in IMOD. Reconstruction of all

406 tomograms was done with IMOD (The Boulder Laboratory for 3D Electron Microscopy of Cells,

407 University of Colorado Boulder, CO) using the back-projection method (35-37) Cryo-tomograms

408 collected on a 4K x 4K camera were binned by 2 to obtain a voxel size of 0.867 nm, to be

409 comparable with the other tomograms. All tomograms were subjected to image filtering

410 (nonlinear anisotropic diffusion filter) to improve contrast.

411

412 **Pectin and hemicellulose removal from *Arabidopsis thaliana***: ~2 mm long stem segments were

413 fixed in 4% paraformaldehyde, 2% glutaraldehyde in 0.03 M phosphate buffer (pH 7.4)

414 containing 0.5mg/ml ruthenium red overnight at 4 °C. Samples were then rinsed in the same

415 buffer and consecutive stem segments from the same plants were treated in parallel with three

416 different treatments: (1) Control - no chemical treatment; (2) 0.5 % ammonium oxalate at 60° C

417 for 48 hours for pectin removal; and (3) pectin removal as (2) followed by 4 % NaOH at RT for

418 96 h to remove the majority of hemicelluloses and any non-cellulosic polysaccharides. All

419 samples were rinsed in distilled water and then fixed in 0.1% osmium tetroxide with 0.5mg/ml

420 ruthenium red for 1 h at RT. The samples were then dehydrated in acetone series and infiltrated in

421 Epon-Araldite resin-acetone series using Leica EM AMW automatic microwave tissue processor.

422 Samples were incubated overnight in 100% resin and then polymerized at 60°C for 2-3 days.

423

424 **Ultrathin sectioning and electron tomography of resin embedded samples:** 150 nm thick

425 sections were cut from resin embedded samples using Leica UC6 ultramicrotome (Leica

426 Microsystems Inc.). All sections were labeled with 5 nm gold fiducials for 4 mins each on both

427 sides followed by several washes in distilled water. The sections were then post stained with 2%

428 uranyl acetate in methanol for 5 mins, followed by Reynold's lead citrate solution for 2 mins.

429 After locating areas of interest, dual axis tilt series were collected from +65° to -65° with 1°

430 increments on a Philips Tecnai F12 TEM (FEI) with 2K x 2K Gatan Ultrascan 1000 CCD camera

431 and SerialEM software (36, 37), at 120 kV accelerating voltage and a voxel size of ~0.8 nm.

432 Images were aligned by tracking the fiducial markers in IMOD. Reconstructions of tomograms

433 were done using the weighted back-projection method in IMOD.

434

435 **Segmentation and image analysis:** Segmentation of all tomograms was done by the 'threshold

436 segmentation' method in Amira (Thermofisher Inc, Hillsboro, OR, USA). A triangular mesh

437 surface was generated in Amira with the 'unconstrained smoothing' option, for visualization and

438 quantitative geometric analysis of the cell wall components. Dimensions of long filamentous

439 structures, the distance (center-to-center) and the shortest gap between the filaments, angle of

440 microfibrils, and the dimensions of short bridge-like cross-links joining the long filaments were

441 measured for each tomogram volume in Amira.

442

443 **Simulation:** Geometry of the ideal models was mostly generated with Matlab (MathWorks, Inc,

444 Natick, MA, USA), mechanical analysis of the numerical models was mainly performed with

445 COMSOL (COMSOL AB, Stockholm, Sweden) and most postprocessing was set up with Python

446 scripts in Paraview (Sandia National Laboratory and Kitware Inc, Los Alamos National

21

447   Laboratory, Los Alamos, NM, USA). Some exceptions were the nonlinear buckling analysis

448   which was performed in ANSYS (Swanson Analysis Systems Inc., Canonsburg, PA, USA), the

449   homogenization of the cell wall and the effect of lignification which was carried out with the

450   Software Geodict (Math2Market GmbH, Kaiserslautern, Germany) as well as the masking of the

451   wall to differentiate hemicellulose out of cellulose, which was conducted with VOXELCON

452   (Quint Corporation, Tokyo, Japan).

453

454   *Mechanical properties of experimental cell wall density maps*

455   We applied homogenization, based on the strain equivalence principle, at different

456   fractions of the measured cell wall, with representative volume elements (RVE) being loaded in

457   different directions (radial, axial, shear forces). Assuming a homogeneous material this test

458   results in predictions of the mechanical properties of entire cell walls. We used a 300x100x50

459   nm RVE, as larger RVEs gave very similar results, whereas smaller RVEs gave substantially

460   different results (Table S1). The suitability of distinct elastic constitutive laws used in the

461   homogenization calculations showed that that average strain equivalence error is low (6%) only

462   in orthotropy, and hence is ideal for modeling the cell walls (Table S2).

463

464   *Ideal models and comparison with the experimental density maps*

465   For our simulations we considered four idealized modeling approaches (Fig. S1): 1) a

466   network model that fully accounts for the 3D volume of both microfibrils and cross-links (NET);

467   2) a simplified version of NET (BEAM), using Timoshenko beam mechanical theory (38-39); 3)

468   a model, with an added a matrix in between the fibers, we call NETMAT; and 4) a model similar

22

469   to NETMAT but without intermicrofibril cross-links, we call MAT. We assumed the same inputs

470   for all four models, and varied the elastic moduli of the interfibrillar matrix from 0.1 to 10 GPa.

471   We calculated the elastic (Young) moduli (radial, longitudinal, tangential and shear), which

472   provides an estimate of the stiffness of the cell wall, as well as the elastic strain energy density

473   stored in the cellulose/hemicellulose and matrix, and compared with the results from the

474   experimental map. Despite having been used frequently in previous computational simulations

475   we found that BEAM vastly underestimates the stiffness mostly because cross-links lengths in

476   this model are highly exaggerated and torsion is not accurately modelled. For NETMAT and

477   MAT, the stiffness increases by up to two orders of magnitude in the transverse direction, with

478   most of the elastic energy being stored in the matrix rather than the fibers, rendering the 3D

479   organization of microfibrils and cross-links nearly meaningless. We chose the NET model for

480   our idealized model simulations. The calculated stiffness in NET (E_R=4MPa, E_T=9 MPa,

481   E_L=1520 MPa) were in good agreement with the homogenized tomography model results, except

482   that the stiffness in the longitudinal (axial) direction was ~25 fold higher (Fig. 4E). However, if

483   tortuosity is considered in the NET model (see below), it has a very limited influence in the

484   radial and transverse directions, but the stiffness drops drastically in the axial direction (E_R=4.5

485   MPa, E_T=9.2 MPa, E_L=63 MPa) bringing it closer to results of SCW-T in all directions. This

486   reinforces the geometrical pattern idealization and the NET approach as a suitable method to

487   model the SCW.

488   ***Introduction of tortuosity into the NET model***

489   The ~25-fold discrepancy in the longitudinal/axial moduli between NET and MAP led us

490   to study the experimental map in more detail. We realized that microfibrils had a somewhat

491   irregular, wavy appearance, with an uneven distribution of hemicellulose along the cellulose

23

492   core, which results in a weakening of the microfibril in the axial direction. We modelled such

493   imperfections by introducing a tortuosity (twist) in our idealized microfibril model. Introduction

494   of tortuosity has a very limited influence in the transverse direction, but results in stiffness drop

495   in the axial direction, which brings E_L in close agreement with the MAP model. We analyzed the

496   implications of tortuosity by performing nonlinear buckling and viscoelastic analyses (Fig. 4H,

497   I). While the buckling load is reduced ~50-fold, tortuous fibers are much more ductile as they

498   can undergo ~9-times larger deformations before collapse in comparison to straight idealized

499   fibers, storing up to 43% more elastic energy than straight fibers as they deform. We conclude

500   that while tortuosity significantly reduces the stiffness of the cell wall, it also increases its

501   ductility as well as the dissipation of elastic and viscoelastic energies, which could be crucial for

502   plants to prevent breakage against extreme loading (such as in high winds).

503   *Mechanical Analysis of NET model*

504   We tested several geometrical features of the NET model, including network size, cross-

505   link arrangement, number of cross-links with the same volume of hemicellulose, the inclination

506   of the cross links as well the orientation of the microfibrils, and found that neither an increase of

507   the height, nor length, nor thickness of the overall network significantly altered the stiffness or

508   the relative elastic energy storage, if the ratio of cross links per length is kept constant,

509   reinforcing the notion that mechanical analysis of relatively small cell wall portions is still

510   relevant for entire cells. Fewer but thicker cross-links promote better load transfer to

511   microfibrils, leading to more evenly distributed strain energy. The inclination of the

512   hemicellulose cross-links had little effect on the overall stiffness.

513

514   Supplemental Material References:

24

515   32. Yakovlev S, Downing KH (2011) Freezing in sealed capillaries for preparation of frozen

516   hydratedsections. J Microscopy 244: 235-247

517   33. Suloway C, Pulokas J, Fellmann D, Cheng A, Guerra F, et al. (2005) Automated molecular

518   microscopy: the new Leginon system. J Struct Biol 151: 41-60

519   34. Mastronarde DN (2005) Automated electron microscope tomography using robust

520   prediction of specimen movements. J Struct Biol 152: 36-51

521   35. Kremer JR, Mastronarde DN, McIntosh JR (1996) Computer visualization of three-

522   dimensional image data using IMOD. J Struct Biol 116: 71-76

523   36. Mastronarde DN (1997) Dual-axis tomography: an approach with alignment methods that

524   preserve resolution. J Struct Biol 120: 343-352

525   37. Timoshenko, S. P., 1921, *On the correction factor for shear of the differential equation for*

526   *transverse vibrations of bars of uniform cross-section*, Philosophical Magazine, p. 744.

527   38. Timoshenko, S. P., 1922, *On the transverse vibrations of bars of uniform cross-section*,

528   Philosophical Magazine, p. 125.
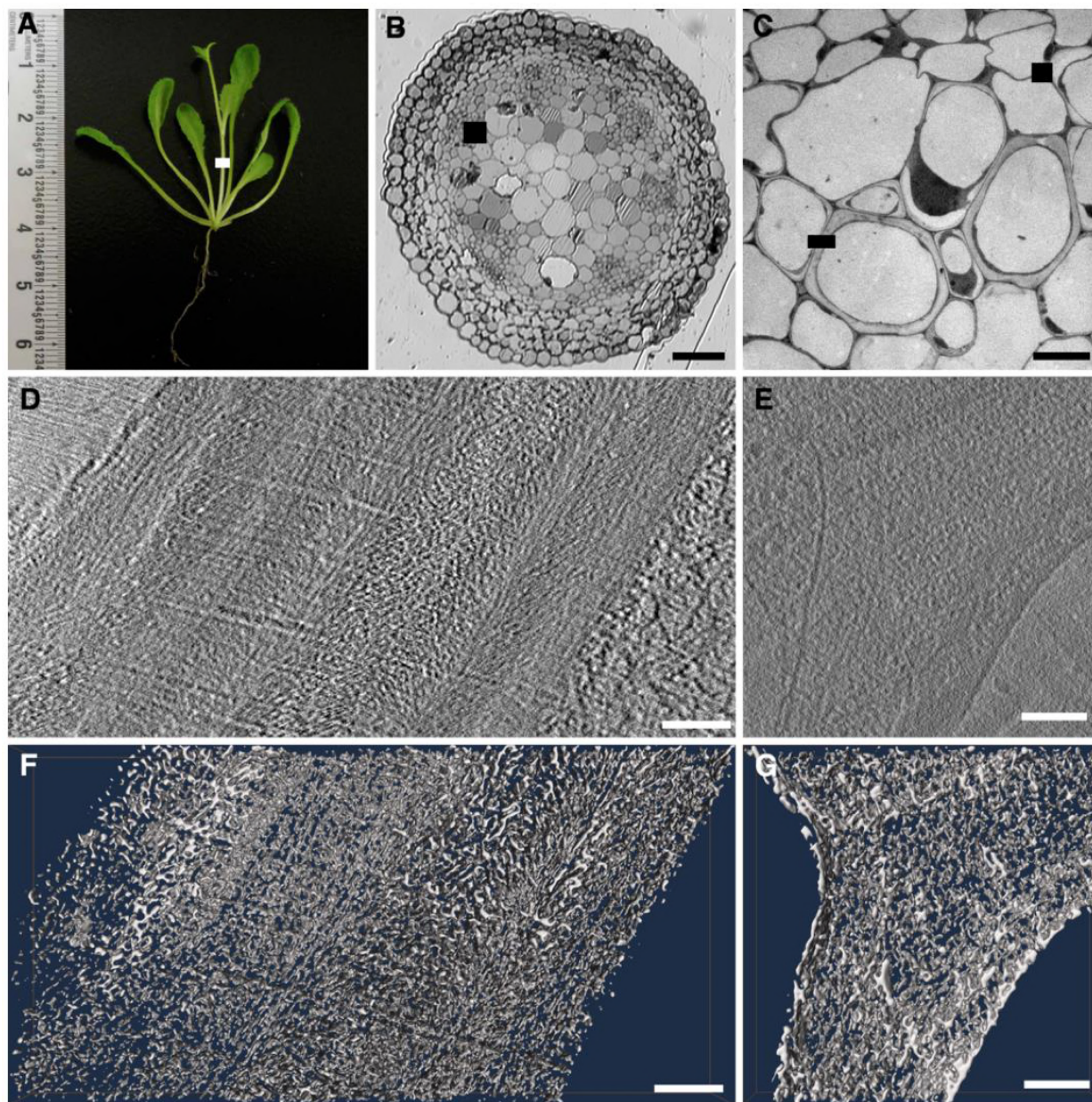
529

530

531

532   Figure 1

533

534

535

536   **Fig 1.** Cryo-electron tomography of thick xylem tracheary elements cell walls and thin xylem

537   parenchyma. A) 1 month-old *Arabidopsis thaliana* inflorescence stem tissue. The white box

26

538   marks a stem segment that was taken for cryo-electron tomography. B) Cross-section through

539   the stem showing the different tissue and cell types in the stem. The black box marks a tissue

540   region similar to the one used for cryo-EM imaging. Note that the section displayed is a Toluene

541   Blue-stained semithin section cut from a high-pressure frozen, freeze-substituted and resin-

542   embedded samples imaged by optical light microscopy in order to provide an overview of the

543   tissues and cells in the plant stem organ. Scale bar = 50 µm. C) Electron micrograph of a ~25 µm

544   by ~25 µm tissue region of interest showing both a thick xylem tracheary elements cell wall (left

545   box) and a thin xylem parenchyma cell wall (right box). Scale bar = 5 µm. D) Zero degree

546   projection view cryo-electron microscopy of thick xylem tracheary elements cell wall, containing

547   primary and secondary cell wall. E) Zero degree projection view cryo-electron microscopy of

548   thin xylem parenchyma cell wall, containing only primary cell wall. F) 3D rendering of a ~50 nm

549   thin slab of a cryo-tomogram of xylem tracheary elements cell wall. G) 3D rendering of a ~50

550   nm thin slab of a cryo-tomogram of xylem parenchyma cell wall. Scale bars = 100 nm.

551

552

553   Figure 2

554
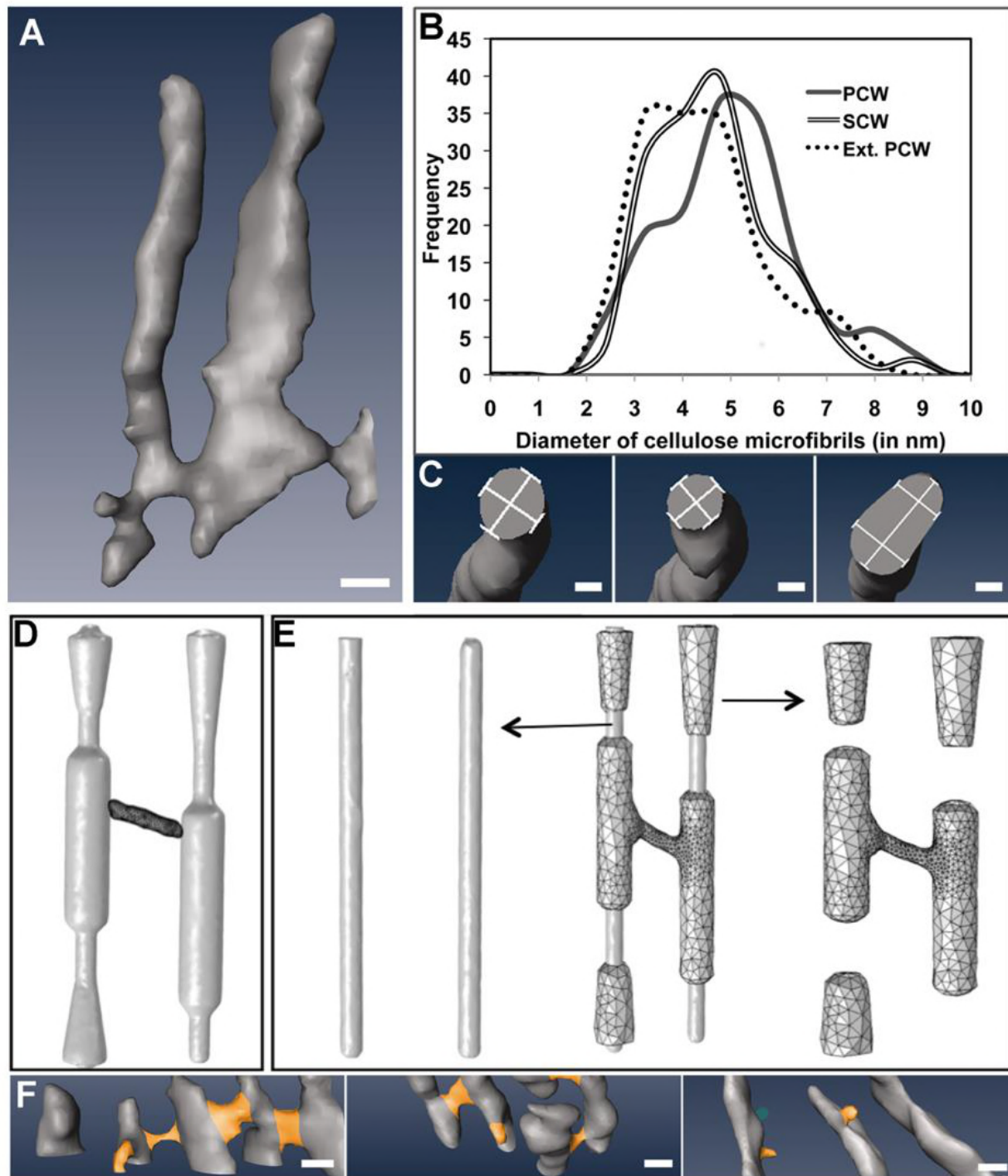
555

556   **Fig 2.** Statistical analysis based 3D modeling of microfibrils and cross-links A) 3D rendering of

557   two neighboring microfibrils in the cryo-tomogram. Scale bar = 5 nm. B) Plot of the statistical

558   analysis of the frequency of microfibril diameter reveals a peak at 3.5 nm and 5-5.5 nm, and a

559   small shoulder to dimensions up to 9 nm. C) Gallery of 3 different microfibrils cross-sections

560   illustrating the numbers obtained in Fig 4B) with microfibrils being round at ~3.5 nm (middle

561   panel), oval shaped with a diameter of ~3.5 nm by ~5-5.5 nm (left panel), reaching up to 9-10

562   nm (right panel). Scale bars = 2 nm. D) Hypothetical 3D-CAD model with all of cellulose

563   residing in the microfibrils and hemicellulose confined to cross-links only. E) Alternative 3D

564   model of two adjacent microfibrils (middle) that contain a cellulose core (left), surrounded by a

565   hemicellulose sheath as well as a cross-connection between adjacent microfibrils (right). F)

566   Occurrence of cross-links in PCW (left), SCW (middle) and chemically extracted PCW (right).

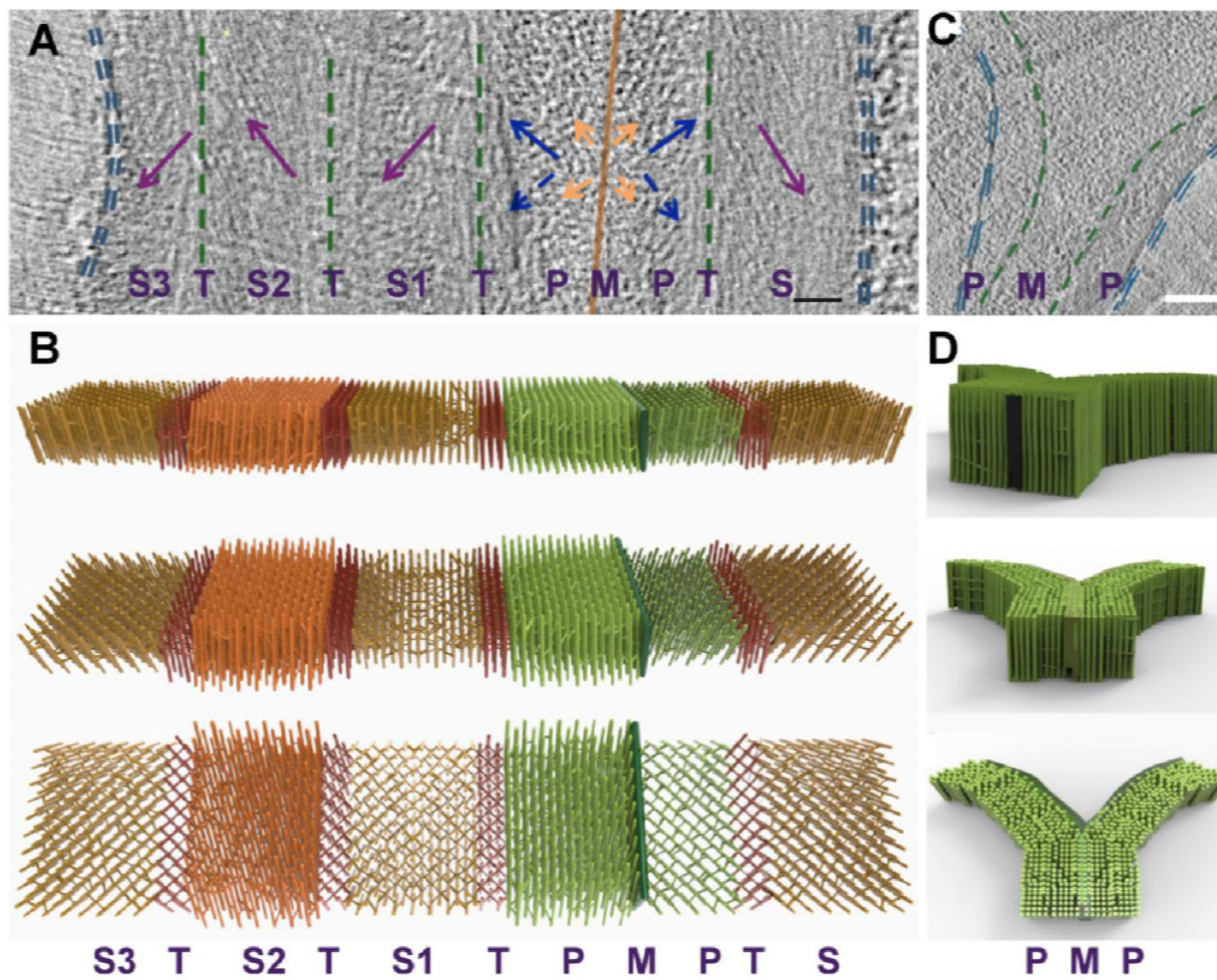567   Scale bars = 5 nm.

568

569

570

571   Figure 3

572

573

574

575 **Fig 3.** Supramolecular 3D organization of microfibrils in xylem tracheary elements and xylem

576 parenchyma cell walls. A) Zero-degree projection image of xylem tracheary elements cell wall,

577 showing two adjacent cells with both secondary and primary cell walls. Note that one of the two

578 adjacent cells has several secondary cell wall subregions, called S1, S2 and S3 and transition

579 zones (T). On the other side of the middle lamella (M) is the primary cell wall P, a transition

580 zone T as well as one secondary cell wall region.Scale bar = 100 nm. B) Idealized model of a

581 xylem tracheary elements cell wall at side view (top), slanted 45˚ view (middle) and an en-face

582 view of microfibrils (bottom). Note that microfibril orientation differs in S1, S2 and S3, with 15

583 layers of microfibril featuring an average angle of minus ~27˚, plus ~27˚ and minus ~27˚ off the

584 longitudinal axis (plant elongation direction). S3, S2, S1 and the Primary Cell Wall (PCW)

585 regions are separated by a three layer-transition zone with axial microfibril orientation. The

586 pectin-rich middle lamella is depicted in the idealized model as a single plane separating the cell

587 walls of two adjacent cells. C) Zero-degree projection image of xylem parenchyma cell walls,

588 showing two adjacent cells with only primary cell walls. Scale bar = 100 nm. D) Idealized

589 model of a xylem parenchyma cell wall at side view (top), D2) slanted 45˚ view (middle) and an

590 en-face view (bottom). Note that in PCW microfibril orientation is mostly axial.

591

592   Figure 4

593
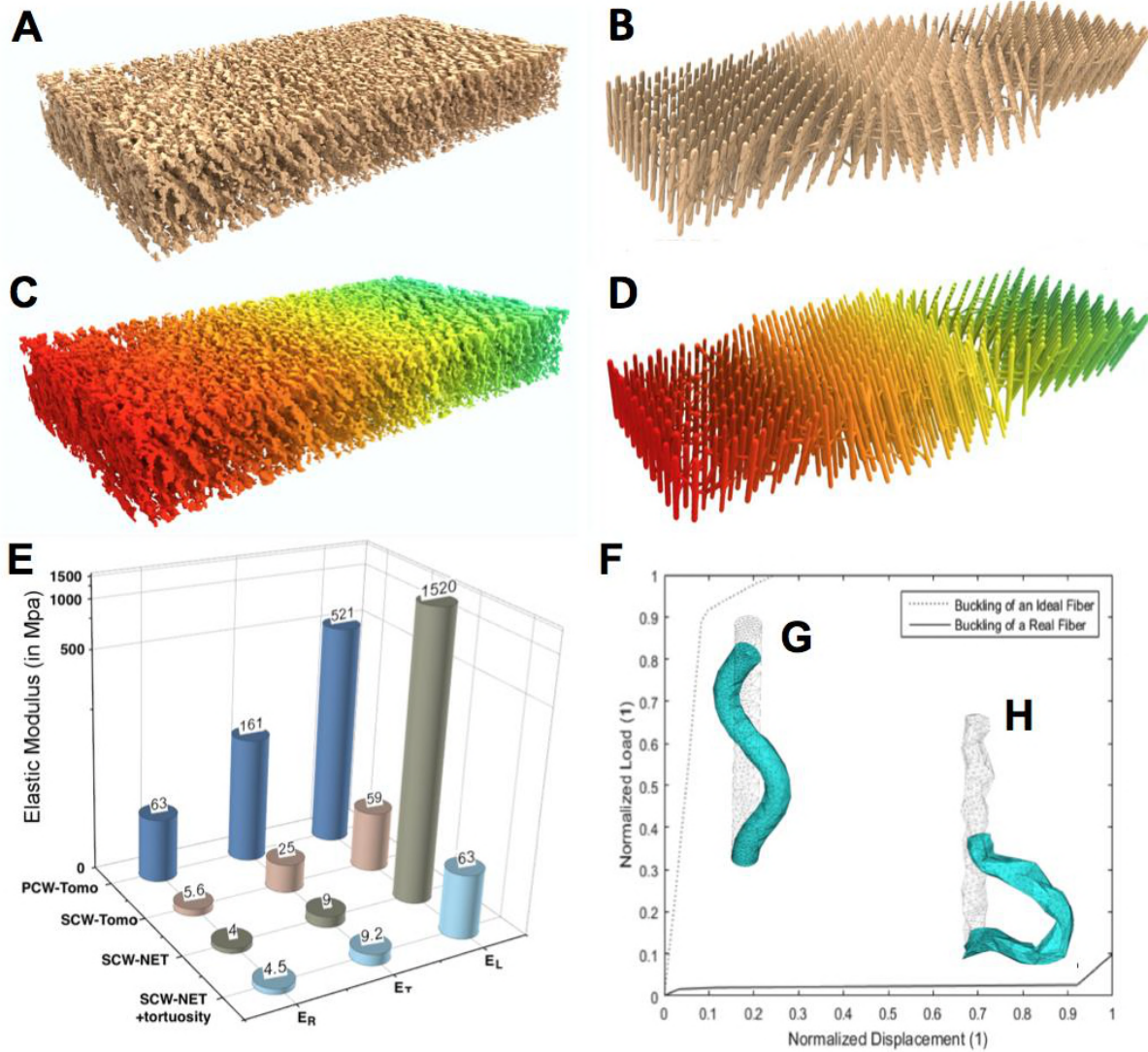
594

595

596

597   **Fig 4.** Computational analysis of cell wall mechanical properties. (A, B) Supramolecular

598   structure segmented from the tomographic reconstruction (A) and a geometrically idealized cell

599   wall model (B) both including only the S1-T-S2-T-S3 portions of the idealized model. (C, D)

32

600   Deformation of the cell wall under radial pressure, for both the segmented volume (C) as well as

601   an idealized model (D), revealing a linear distribution of force throughout the secondary cell

602   wall. (E) Graphic depiction of the Young elastic moduli (radial, longitudinal and tangential) for

603   primary cell walls, secondary cell wall regions segmented from the tomographic 3D data as well

604   as idealized models of the secondary cell walls, before and after introduction of tortuosity. (F, G,

605   H) Load bearing behavior of microfibrils under buckling due to axial stress, revealing significant

606   decrease of failure load but very high increase of ductility (F), when moving from an idealized

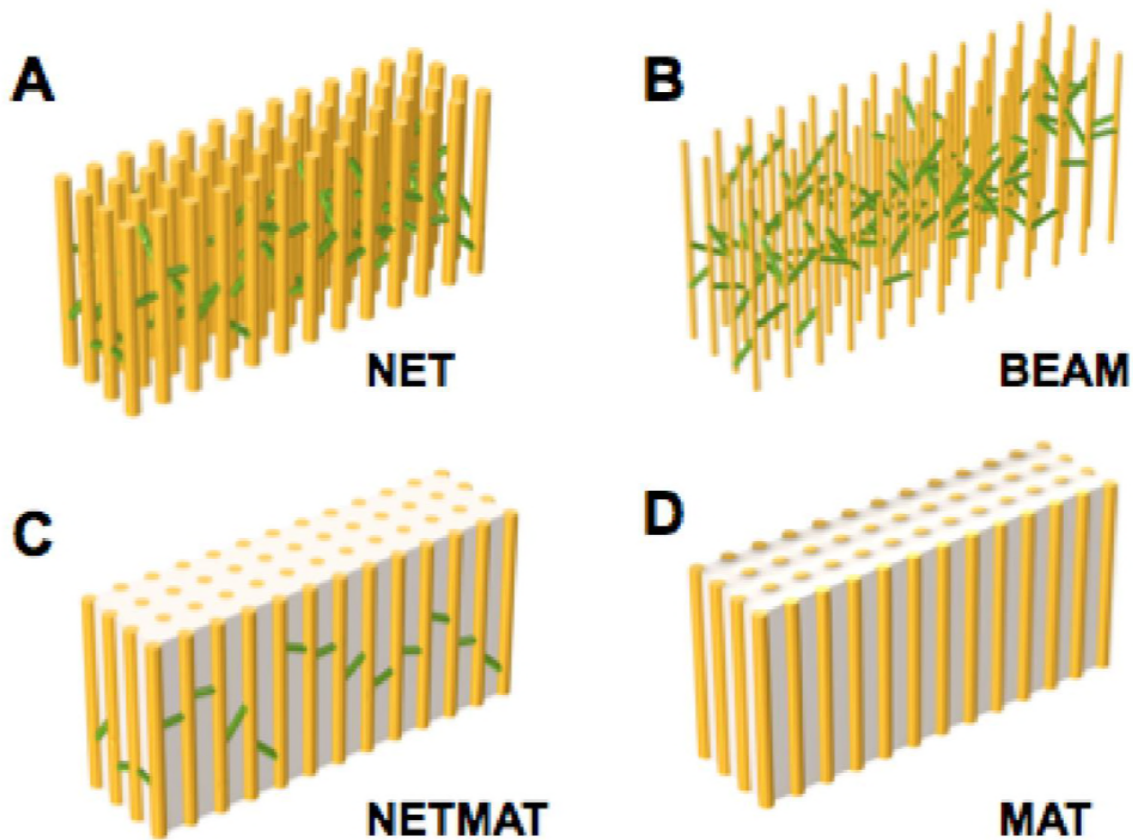607   straight microfibril (G) to a tortuous fiber (H).

608

609

610   Suppl. Figure 1

611

612

613   **Fig S1.** Choice of Modeling Approach. We considered four idealized modeling approaches: (A)

614   NET is a network model that fully accounts for the 3D volume of both microfibrils and cross-

615   links B) BEAM is a simplified approach based on Timoshenko beam mechanical theory (C)

616   NETMAT is similar to NET, with an added a matrix in between the fibers and (D) MAT, which
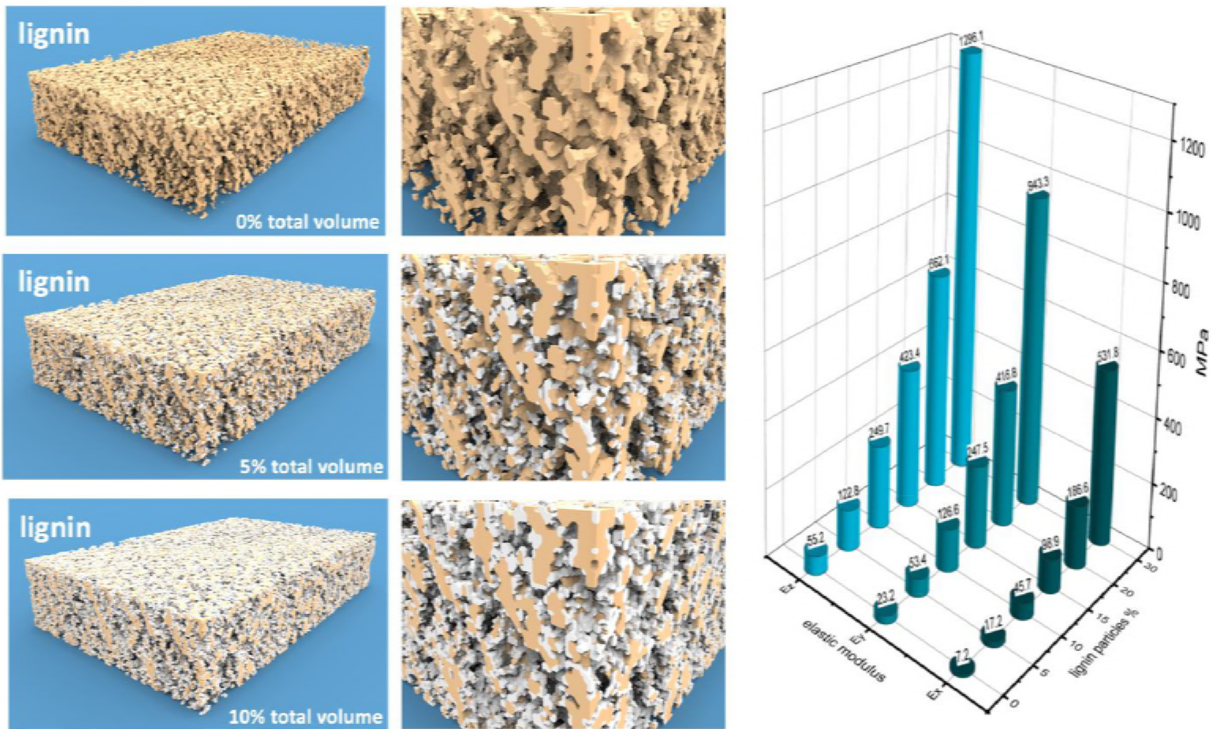
617   is similar to NETMAT but does not contain inter-microfibrillar cross-connectors.

618

619

620   Suppl. Figure 2

621

622

623

624   **Fig S2.** Modeling of lignin distribution in secondary cell wall (A, D) Secondary cell wall with an

625   assumed 0% lignin. 20% of the total volume available is occupied by the cellulose/hemicellulose

626   network. (A) overview (D) close-up detail. (B, E) 5% total volume of lignin (equivalent to a 15-

627   20% dry weight) is added to the segmented map displayed in A. (B) overview and (E) close-up

628   detail reveal vast amount of space remains unoccupied, inconsistent with a dense matrix in which

629   microfibrils are embedded and thus mechanically connected. Increasing the lignin to 10% of total

630   volume (resulting in a ~30-35% dry weight) leads to much more densely connected network,

631   which is consistent with a matrix at these much higher lignin content. (C) overview (F) close-up

632   detail. Note that the corresponding dry-weight is an estimate making assumptions on similarity in
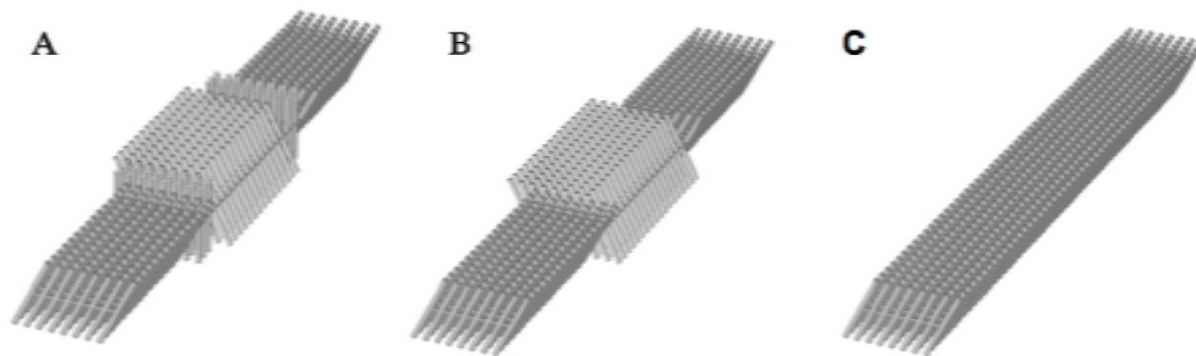
633   density of lignin and cellulose/hemicellulose matrix. (G) Comparison of elastic moduli for radial

634   (Er), tangential (Et) and longitudinal (EL) force loading.

635

636

637

638   Suppl. Figure 3

639

640   **Fig S3.** Hypothetical XTE cell wall models with varying supramolecular organization. A) Cell

641   wall model with 15 microfibril layers each in the S1, S2 and S3 SCW that were inclined minus

642   27˚, plus 27˚ and minus 27˚, respectively, and that were separated from each other by a 3

643   microfibril layer transition zone with axial microfibril orientation. B) Cell wall model without

644   transition zones, and 18 layers of microfibrils that are minus/plus/minus 27˚ inclined. C) All

645   microfibrils (54 layers) are all inclined by 27˚.

646